International Journal of Minerals, Metallurgy and Materials
Volume 28, Number 9, September 2021, Page 1534
https://doi.org/10.1007/s12613-020-2113-1

Characterization of MCrAlY/nano-Al_2O_3 nanocomposite powder produced by high-energy mechanical milling as feedstock for high-velocity oxygen fuel spraying deposition

F. Ghadami, A. Sabour Rouh Aghdam, and S. Ghadami

Department of Materials Engineering, Tarbiat Modares University, P.O. Box 14115-143, Tehran, Iran
(Received: 23 March 2020; revised: 27 May 2020; accepted: 1 June 2020)

Abstract: Al_2O_3 nanoparticles and MCrAlY/nano-Al_2O_3 nanocomposite powder (M = Ni, Co, or NiCo) were produced using high-energy ball milling. The MCrAlY/nano-Al_2O_3 coating was deposited by selecting an optimum nanocomposite powder as feedstock for high-velocity oxygen fuel thermal spraying. The morphological and microstructural examinations of the Al_2O_3 nanoparticles and the commercial MCrAlY and MCrAlY/nano-Al_2O_3 nanocomposite powders were investigated using X-ray diffraction analysis, field-emission scanning electron microscopy coupled with electron dispersed spectroscopy, and transmission electron microscopy. The structural investigations and Williamson–Hall results demonstrated that the ball-milled Al_2O_3 powder after 48 h has the smallest crystallite size and the highest amount of lattice strain among the as-received and ball-milled Al_2O_3 owing to its optimal nanocrystalline structure. In the case of developing MCrAlY/nano-Al_2O_3 nanocomposite powder, the particle size of the nanocomposite powders decreased with increasing mechanical-milling duration of the powder mixture.

Keywords: MCrAlY; Nanocomposite powder; High-energy mechanical milling; Williamson–Hall analysis; HVOF coating

1. Introduction

In recent decades, diffusion and overlay thermal protective coatings have been utilized to save parts and equipment from corrosion and oxidation at high temperatures [1]. From this point of view, thermally sprayed coatings based on MCrAlY (M = Ni, Co, or NiCo) alloys were widely applied on gas turbines and aero-engines to protect superalloy blades and related components against hot corrosion and oxidation during service [2–8]. Following the enhancement of the sustainability of MCrAlY from oxidation attacks, its mechanical and erosion properties must be preserved to an optimum level [9–13]. Recently, several works have focused on the thermal stability and structural attributions of MCrAlY powders and their developed coatings using micro- and/or nano-scale metallic, carbide, or oxide additives [14–16], applying post spray treatments [7,17–21], modification with spark plasma sintering [22–25], and remelting of coated parts [14,26–27].

High-energy ball milling is a practical method for developing oxide nanoparticles and oxide dispersion-modified composite powders [28–33]. Li *et al.* [34] investigated the effect of a fine dispersion of Al_2O_3 on the wear resistance of NiCoCrAlY coatings at high temperatures. They found that the mean friction coefficient of the modified MCrAlY coatings is lower than that of the original MCrAlY coating at similar wear parameters. Khodsiani *et al.* [35] developed NiCoCrAlYSi/nano-Al_2O_3 nanocomposite feedstock powder by using cryomilling. They concluded that the average size of nanocomposite agglomerates accordingly increases with prolonged milling time for NiCoCrAlYSi feedstock powder, but the mean particle size distribution following cryomilling decreases with the addition and dispersion of Al_2O_3 nanoparticles onto the powder.

Ghadami *et al.* [30] prepared NiCoCrAlY/nano-CeO_2 nanocomposite powder by using the planetary ball milling. They reported that homogeneous nanocomposite powder may be attained after 15 h of mechanical milling by adding about 1.0wt% ethanol as a process control agent (PCA). Mahesh *et al.* [36] and Kamal *et al.* [37] produced NiCrAlY–0.4wt% CeO_2 (micron-sized) composite powder by using ball milling. They reported that the modified coating applied via thermal spraying shows better oxidation resistance than the as-received NiCrAlY coating. The addition of oxide nanoparticles in MCrAlY powder may affect the fracturing pro-

Corresponding authors: F. Ghadami E-mail: f.ghadami@modares.ac.ir; A. Sabour Rouh Aghdam E-mail: sabour01@modares.ac.ir

cess of the milled powder (e.g., fracture under severe plastic deformation) and cause grain refining in the nanocomposite powder during mechanical milling. The steady-state conditions for producing nanocomposite powder may be attained accordingly in a short milling time [35].

Numerous investigations focused on the preparation and characterization of micro- and nano-scale Al_2O_3 modified MCrAlY alloys, powders, and coatings. In addition, considerable examinations used commercial-grade nanoparticles to develop nanocomposite powders. Studies about the structural characteristics of MCrAlY powder feedstock reinforced by distributed ceramic nanoparticles are still not widely available. Limited research also analyzed the preparation and the morphological and structural properties of MCrAlY/nano-Al_2O_3 nanocomposite powder by using high-energy ball milling. Therefore, the present study analyzed the structural and morphological features of the developed Al_2O_3 nanoparticles by performing microscopic examinations, and the obtained results were verified using Williamson–Hall analysis. The dispersion state of the Al_2O_3 nanoparticles into the NiCoCrAlY powder and the effect of milling parameters on the oxide dispersion and morphology of the nanocomposite powder were discussed in detail. This study aimed to prepare nano-sized Al_2O_3 and develop MCrAlY/nano-Al_2O_3 nanocomposite feedstock powder for use in high-velocity oxygen fuel (HVOF) thermal spraying. HVOF spraying was utilized to develop MCrAlY coatings on Ni-based superalloy substrates. The structural characteristics of the processed MCrAlY/nano-Al_2O_3 powders and developed coatings were also investigated and discussed in detail.

2. Experimental

2.1. Materials

Commercial-grade spheroidal MCrAlY (NiCoCrAlY) powder with the composition of Ni(bal.)–20wt%Co–14wt%Cr–12wt%Al–0.5wt%Y from Amdry 365-1 (Oerlikon-Metco, USA) was utilized as the base powder. Commercial-grade micro-scale Al_2O_3 powder (99.9% purity, Sigma-Aldrich, USA) was also used as the starting powder for the development of nano-Al_2O_3. The characteristics of the powders used are listed in Table 1. Nickel-based Inconel 738LC superalloy plates were used as the substrate for applying the commercial and nanocomposite coatings.

Table 1. Characteristics of NiCoCrAlY powder feedstock, micron-sized Al_2O_3, and nano-Al_2O_3 oxide dispersion

Powder	Powder size	Manufacturing process	Product code	Powder morphology	Manufacturer company
NiCoCrAlY	(−45 + 5) μm	Gas atomized	AMDRY 365-1	Spheroidal	Oerlikon-Metco
Al_2O_3	≤2 μm	—	265497	Crashed	Sigma-Aldrich
Nano-Al_2O_3	(30–60) nm	Developed	—	Irregular	—

2.2. Nano-sized and nanocomposite powder processing

At the first stage, Al_2O_3 nanoparticles were prepared using mechanical milling under a rotational speed of 300 r/min up to 48 h. Al_2O_3 nanoparticles were obtained using mechanical milling using stainless steel cups and balls in accordance with our previous investigations [30,38]. Iron contamination is inevitable for the ball-milled Al_2O_3 oxides because of the wear of stainless steel balls and cups by hard oxide particles. Therefore, the milled powders were leached by cleaning with diluted nitric acid and subsequent washing with distilled water. At the second stage, 1.0wt% of developed Al_2O_3 nanoparticles were added to the MCrAlY powder to obtain homogeneous MCrAlY/nano-Al_2O_3 nanocomposite powders. The powder mixture was mechanically milled using a high-energy planetary ball-milling apparatus. Mechanical milling was performed for 5, 15, 25, and 35 h under inert Ar atmosphere to prevent undesirable oxidation and to obtain relatively uniform nanocomposite powders. In this case, a small amount of ethyl alcohol (about 1.0wt%) was also added to the milling mixture as a PCA to prevent excessive agglomeration. The milling was interrupted every 1 h to minimize the temperature increase and possible oxidation of the nanocomposite mixture. The detailed preparation process for nano-Al_2O_3 powders was presented in our previous investigations [20,30–31,38–39]. The main mechanical-milling parameters for developing MCrAlY/nano-Al_2O_3 nanocomposite powder are presented in Table 2.

Table 2. Process parameters of ball milling to obtain NiCoCrAlY/nano-Al_2O_3 nanocomposite powders

Milling medium	Periodic rest time / ($min \cdot h^{-1}$)	PCA (ethyl alcohol) / wt%	Rotational speed / ($r \cdot min^{-1}$)	Ball-to-powder mass ratio	Milling duration / h
Ar atmosphere	5	1.0	250	20:1	5, 15, 25, and 35

2.3. HVOF thermal spray deposition

HVOF spraying equipment (MEC, India) with propane/oxygen system was utilized to apply (200 ± 50) μm of the conventional MCrAlY and MCrAlY/nano-Al_2O_3 nanocomposite coating taken from the commercial and optimized nanocomposite powders on grit-blasted nickel-based superalloy substrates. All nanocomposite powders were sieved to 30–60 μm to obtain suitable powder feedstock quality for

HVOF spraying. The developed depositions included two types of MCrAlY coatings reinforced by nano-Al_2O_3 with different powder feedstock preparations and one MCrAlY coating without nanoparticles. For this case, HVOF spraying parameters were set at the following optimized levels: propane and O_2 gas flow, 55 and 210 L/min; carrier gas flow, 20 L/min. For this case, the powder feed rate was 35 g/min, and the stand-off distance was 28 cm.

2.4. Characterization techniques

The morphological properties of the MCrAlY/nano-Al_2O_3 nanocomposite powders were evaluated using field-emission scanning electron microscopy (FESEM) coupled with energy dispersive spectroscopy (EDS). Moreover, transmission electron microscopy (TEM) was also utilized to detect nano-scale oxides in the MCrAlY/nano-Al_2O_3 nanocomposite powder.

Structural properties of the as-received MCrAlY and MCrAlY/nano-Al_2O_3 nanocomposite powders were investigated via X-ray diffraction (XRD) with Cu K_α radiation (λ = 0.154056 nm) at 40 kV and 40 mA (X'pert, Phillips, Netherlands). Obtained diffraction patterns were indexed and then verified in accordance with the International Center for Diffraction Data bank. Simultaneously, the crystallite size and strain of Ni- and Co-rich γ-phase for all types of the as-received and nanocomposite powders under different milling times were calculated using the width of major γ-phase peaks from the corresponding XRD patterns [40]. The powder crystallite size D_c can be obtained by the Williamson–Hall plot (Eq. (1)):

$$\beta \cdot \cos(\theta) = k \cdot \lambda / D_c + \eta \cdot \sin(\theta) \quad (1)$$

where β is the full width at half maximum (FWHM) value (radians), θ is the diffraction angle (radians), k is the shape factor (~0.91), λ is the wavelength of the Cu K_α radiation (nm), and η is the percentage of lattice strain (%). In addition, the crystalline size of the powders (D_c) can be calculated by extrapolating the value of sin(θ) to zero to eliminate the lattice strain or distortion effect.

3. Results

3.1. Development of Al_2O_3 nanoparticles

The powder morphology and EDS elemental analysis of the nano-scale Al_2O_3 powders are presented in Fig. 1. Secondary electron FESEM images of the nano-sized Al_2O_3 (Figs. 1(a) and 1(b)) show that each agglomerated oxide powder includes numerous nano-sized alumina. In this regard, results of elemental analysis by EDS (Fig. 1(c)) also indicated that the mechanically milled Al_2O_3 powders had anticipated compositions but were almost free from Fe-based contamination after ball milling.

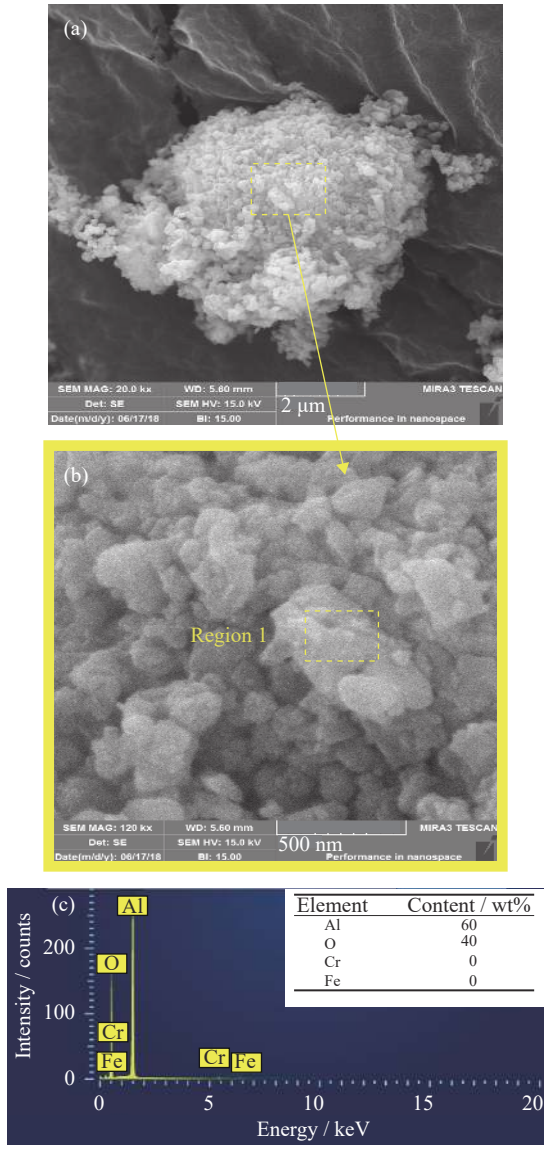

Fig. 1. High-resolution secondary electron images of Al_2O_3 nanoparticle agglomerate synthesized using ball milling after 48 h under two different magnifications (a, b), as well as EDS analysis of region 1 for nano-Al_2O_3 powder (c).

XRD patterns of the commercial and high-energy ball-milled Al_2O_3 powders after 24 and 48 h are shown in Fig. 2. For all types of the commercial and ball-milled Al_2O_3 powders, the diffraction patterns were only justified to the α-Al_2O_3 phase. Hence, no other phases (e.g., Fe-based compounds) were detected from the XRD of the powders. This result indicated that the possible Fe-based contamination was satisfactorily eliminated using the subsequent acid cleaning process after mechanical milling. The peak broadening of the milled powders might be associated with the extreme decrease in grain size compared with the commercial Al_2O_3 powder. This phenomenon may justify the achievement of the Al_2O_3 nanoparticles after high-energy ball milling.

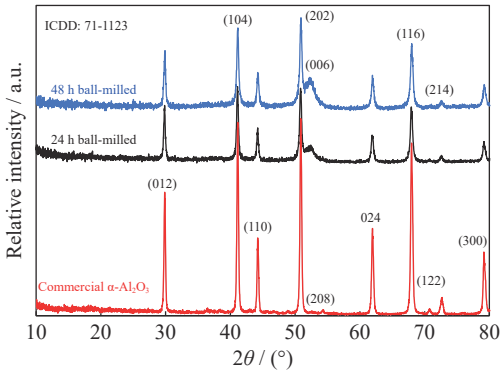

Fig. 2. XRD patterns of the commercial-grade (micron-sized) and nano-sized α-Al_2O_3 powders after 24 and 48 h of ball milling.

3.2. Williamson–Hall analysis of nanoparticles

Calculations of the crystalline size and strain value based on the Williamson–Hall method are shown in Fig. 3. The Williamson–Hall plots of FWHM $\beta\cos(\theta)$ versus $\sin(\theta)$ for the commercial and ball-milled Al_2O_3 powders (Fig. 3(a)) indicated that the crystallite size can be obtained from the intercept of the straight trend line and $\beta\cos(\theta)$ axis. The low slope of the trend line in the commercial Al_2O_3 powder indicated the minimum amount of strain. The slope of the trend lines increased as the ball-milling duration was prolonged to 12, 24, and 48 h because of the production of a high amount of strain induced by severe plastic deformation during ball-milling. Other related investigations on the calculations of crystallite size support this fact [40–41].

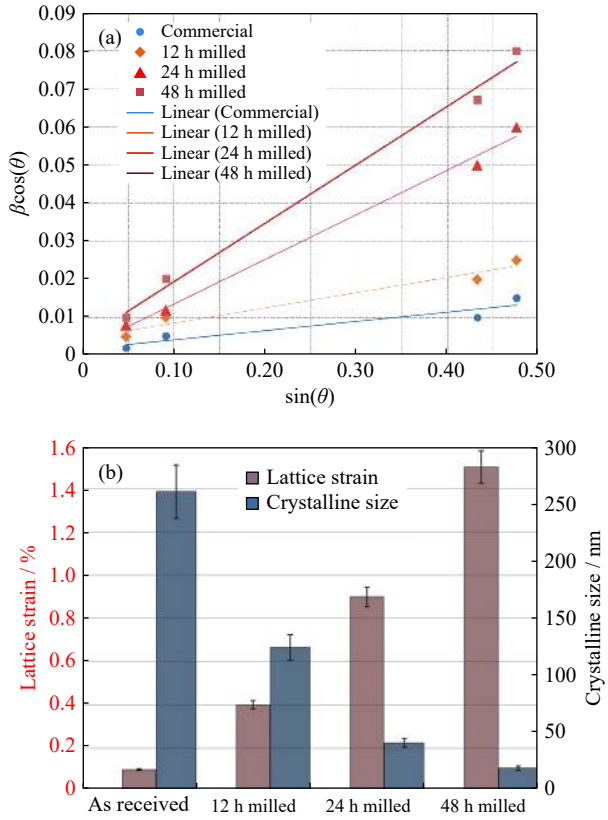

Fig. 3. Williamson–Hall plot of FWHM $\beta\cos(\theta)$ versus $\sin(\theta)$ for Al_2O_3 nanoparticles after 12, 24, and 48 h of ball milling (a) and comparative values of lattice strain percentage and crystalline size calculated using the Williamson–Hall method for ball-milled Al_2O_3 nanoparticles after 12, 24, and 48 h of milling (b).

Fig. 3(b) indicates the lattice strain percentage and crystalline size of the commercial and ball-milled Al_2O_3 powders. The minimum lattice strain in the commercial Al_2O_3 can be attributed to the production method of commercial powder (crashed), which may reduce and/or eliminate the lattice strain. By contrast, the ball-milled Al_2O_3 powders after 12, 24, and 48 h have a considerable amount of lattice strain. The plastic deformation during high-energy ball milling and powder crashing and agglomeration is the main causes of residual lattice stress/strain in the ball-milled powders. As shown in Fig. 3(b), the crystalline size of Al_2O_3 extremely decreased from 130 to 40 nm when the milling time was prolonged, producing Al_2O_3 nanoparticles.

3.3. Characterization of the nanocomposite powders

Fig. 4 shows the high-resolution FESEM images (secondary electron mode) of the morphology of the as-received commercial (Figs. 4(a)) and 4(b), mechanical-milled MCrAlY nano-Al_2O_3 powders after 5 h (Figs. 4(c) and 4(d)), 15 h (Figs. 4(e) and 4(f)), and 25 h (Figs. 4(g) and 4(h)) of milling process. The commercial MCrAlY powder has a spheroidal morphology because it was produced using a gas-atomized method. Otherwise, the ball-milled MCrAlY/nano-Al_2O_3 nanocomposite powder after 5 h shows a relatively semi-spherical and bulky disk morphology (Fig. 4(d)). Formation of the powder with this morphology arises from the stress caused by severe ball and powder contact during the first stages of the milling process. As the duration of ball milling was prolonged, the value of processing stress increased while the morphology of the nanocomposite powder transferred to flaky morphology because of plastic deformation (Fig. 4(e)). The continuous collisions among the processed MCrAlY/nano-Al_2O_3 nanocomposite powder particles, steel balls, and vial walls caused excessive severe plastic deformation, flaking, cold welding, breakage, and agglomeration of nanocomposite particles through the different periods of mechanical milling [35,42–43]. The morphology of the ball-milled MCrAlY/nano-Al_2O_3 powder after 25 and 35 h became completely flaky compared with the other types of ball-milled powder (Figs. 4(h) and 4(j)).

At a certain lattice strain level, a relatively fine structure network consisting of stress-induced dislocations and low-angle grain boundaries may appear as the duration of ball milling is prolonged [28–29,44]. Simultaneously, low-angle grain boundaries transformed into a nano-scale/amorphous

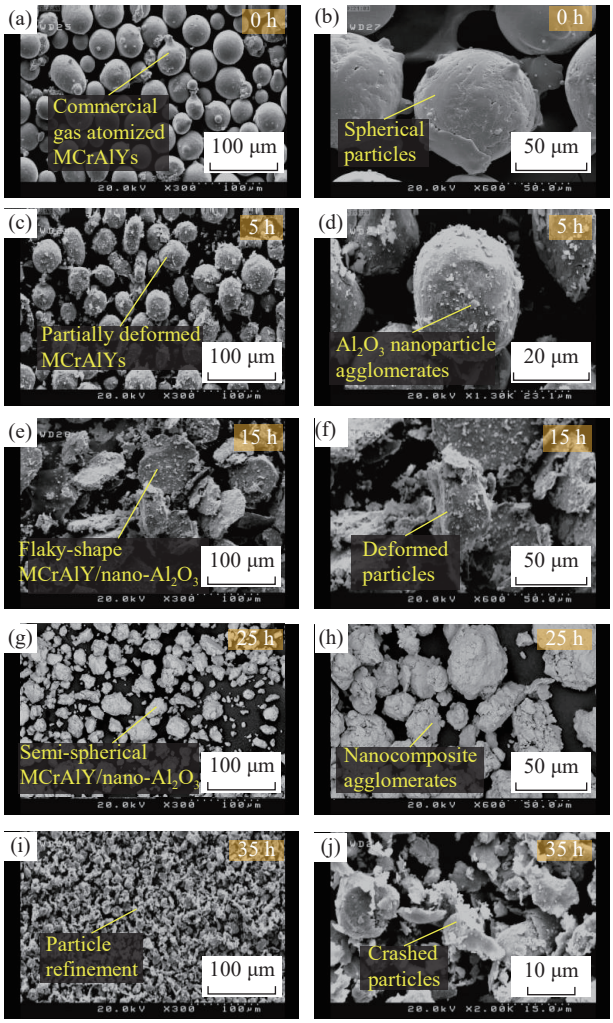

Fig. 4. Secondary electron images of the as-received (a, b) and high-energy ball-milled MCrAlY/nano-Al_2O_3 nanocomposite powders after 5 h (c, d), 15 h (e, f), 25 h (g, h) and 35 h (i, j) of milling time under 250 r/min.

structure with random orientations as the milling duration was prolonged. For this reason, the grain size of the processed powder continuously decreased during ball milling until the last stage (25 h) that the size was saturated at a constant level [42].

Fig. 5 depicts the elemental mapping analysis extracted from an MCrAlY/nano-Al_2O_3 nanocomposite powder particle after 5 h of ball milling (obtained from Fig. 4(d)). As shown in the figure, each MCrAlY/nano-Al_2O_3 nanocomposite particle had a uniform distribution of nano-Al_2O_3 (see Al and O mapping distribution). The average particle size and morphology state versus ball-milling process duration (up to 25 h) for the MCrAlY/nano-Al_2O_3 nanocomposite powder are presented in Fig. 6. The commercial MCrAlY powder had a mean particle size of 45 μm, which was higher than that of ball-milled MCrAlY/nano-Al_2O_3 nanocomposite powder. Besides, by increasing the milling time, the average particle size of the nanocomposite powders decreased from

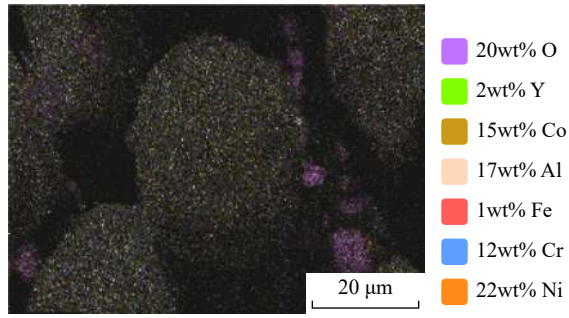

Fig. 5. Elemental mapping analysis of MCrAlY/nano-Al_2O_3 nanocomposite powder after 5 h ball milling (results were obtained from Fig. 4(d)).

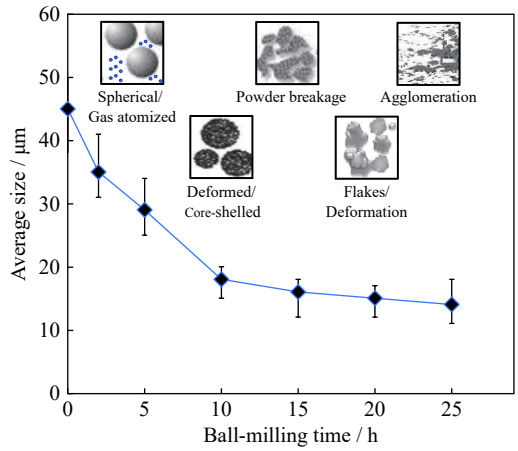

Fig. 6. Average particle size and morphology versus ball-milling duration for MCrAlY/nano-Al_2O_3 nanocomposite powder.

28 μm after 5 h of ball milling to less than 10 μm after 25 h of ball milling.

Fig. 7 shows bright field (BF) and dark field (DF) TEM images of MCrAlY/nano-Al_2O_3 nanocomposite powder after 25 h of ball milling. The BF TEM image (Fig. 7(a)) showed that each nanocomposite powder consisted of partially agglomerated and deformed MCrAlY particles as well as dispersed nano-Al_2O_3 oxide nanoparticles. The selective area diffraction (SAD) pattern in Fig. 7(c) shows that the diffraction points were indexed accordingly and represented a γ (Ni) matrix in the nanocomposite powder. Furthermore, relatively broad and thick diffraction rings in the corresponding SAD pattern can be detected because of the formation of a nano-scale structure in the ball-milled MCrAlY/nano-Al_2O_3 nanocomposite powder. Accordingly, the nano-scale structure of the nanocomposite powder can be further confirmed by DF TEM.

3.4. Characterization of the sprayed coatings

Fig. 8 indicates the backscattered electron modes of the cross-section of MCrAlY coatings with and without nano-Al_2O_3 reinforcement. In addition, secondary electron modes

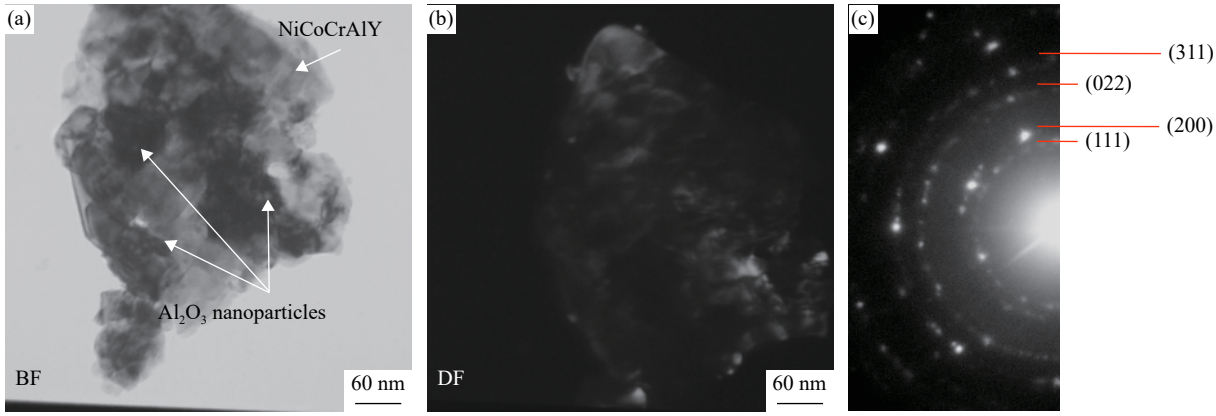

Fig. 7. TEM images of the MCrAlY/nano-Al_2O_3 nanocomposite powder after 25 h of ball milling: (a) bright-field image; (b) dark-field image; (c) corresponding SAD pattern representing Ni-based γ phase in the nanocomposite powder.

of the surface morphology of the conventional MCrAlY and MCrAlY/nano-Al_2O_3 nanocomposite coatings produced with different types of powder feedstock are presented in Fig. 9. As shown in Fig. 8, the average thickness of the sprayed coatings with and without nano-Al_2O_3 is approximately 200 μm. Furthermore, all depositions have relatively similar structural characteristics, demonstrating that the lamellar structure is due to the development of the coating layer by the contact and solidification of fully melted, semi-, or unmelted particles onto the surface, which is the typical structure of thermally sprayed coatings. As shown in Figs. 8(a) and 8(b), the conventional MCrAlY coating represents a considerable amount of unmelted particles as well as structural porosity and oxides. The corresponding unmelted particle also can be

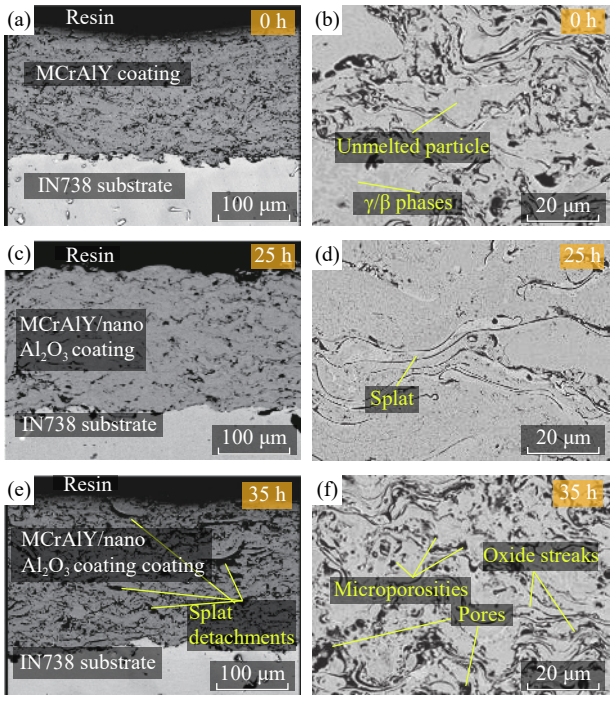

Fig. 8. Backscattered images of the cross-section of HVOF-sprayed conventional MCrAlY coating (a, b) and MCrAlY/nano-Al_2O_3 nanocomposite coating deposited using powder ball milling after 25 h (c, d) and 35 h (e, f) under 250 r/min.

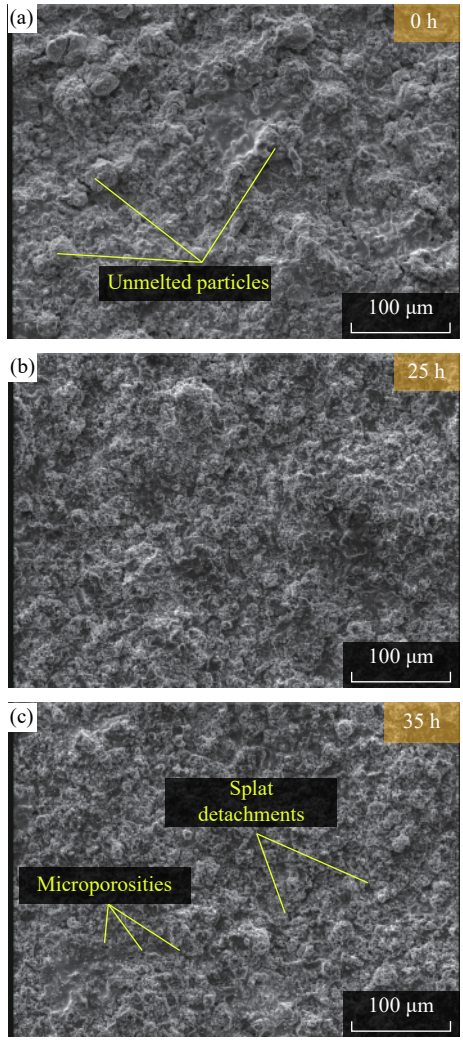

Fig. 9. Secondary electron micrographs of the surface of the HVOF-sprayed conventional MCrAlY coating (a), MCrAlY/nano-Al_2O_3 nanocomposite coating deposited using powder ball milling for 25 h (b) and 35 h (c) under 250 r/min.

observed from the coating surface, as shown in Fig. 9(a). Regions representing splat detachments were also detected for this type of coating.

For comparison, the cross-sectional image of the MCrAlY/nano-Al_2O_3 coating applied from feedstock after 25 h of ball milling shows a relatively denser structure and lower amounts of porosity and oxide contents compared with other types of conventional and nanocomposite coatings (Figs. 8(c) and 8(d)). The surface morphology of the mentioned coating was also more uniform than that of other counterparts (Fig. 9(b)). Conversely, the cross-sectional image of the MCrAlY/nano-Al_2O_3 nanocomposite coating produced from nanocomposite powder after 35 h of ball milling (Figs. 8(e) and 8(f)) shows the worst microstructure with a considerable amount of porosity and oxide stringers.

4. Discussion

4.1. Powder processing

The average particle size and the morphology of the powder are essential parameters that could be used to evaluate the characteristics of powder feedstock for MCrAlY-based powder applications (e.g., as a feedstock for thermal spray deposition techniques) [45]. After ball-milling of the conventional NiCoCrAlY and nano-Al_2O_3 powders, the powder particles experienced about ~85% decrease in its crystalline size, even though the microstructure of the processed powders was reduced to a nanocrystalline regime. In this case, appropriate powder morphology suitable for HVOF deposition is mainly consists of a spherical or semi-spherical morphology with a particle size distribution between 15 and 50 μm [38,42].

As shown in Fig. 4, the particle size of the MCrAlY/nano-Al_2O_3 nanocomposite powders differs at various milling durations. Therefore, the MCrAlY/nano-Al_2O_3 nanocomposite powders obtained after 35 h of milling (Figs. 4(i) and 4(j)) were not applicable to use in the powder feeder system for thermal spraying. The particle size distribution and morphology of the nanocomposite powder are basically affected by milling parameters.

At the initial stages of the milling process to obtain nanocomposite powder, Al_2O_3 nanoparticle agglomerates surrounded each metallic NiCoCrAlY powder. Then, plastic deformation and cold welding of powder particles can progressively occur. At the middle stage of milling, the balance between breakage and joining of the powder particles results in powders with agglomerated morphology. Under this milling condition, the joining of fine particles and the breakage of work-hardened powders can simultaneously occur. Similar statements based on ball-milling conditions were also reported by Sachan and Park [46] and Tahari *et al.* [42]. As shown in Figs. 4(c) and 4(d), the metallic powder particles underwent a partial deformation while nano-Al_2O_3 agglomerates distributed and adhered to the surface of each powder after 5 h of mechanical milling. The processed powder mixture gradually deformed and their morphology changed to flattened/flaky shapes as the milling duration was prolonged to 15 h (Figs. 4(e) and 4(f)). As displayed in Fig. 4(e), stakes of the spalls were also detectable on the flake surface. At the mentioned stage of mechanical milling, particle breakage and fracture mechanism dominated over cold welding. Progressively, the small fragments became bulky or semi-spherical agglomerates with a rough surface as the milling time was prolonged from 15 h to 25 h (see Figs. 4(g) and 4(h)).

From another point of view, the addition of Al_2O_3 nanoparticles to NiCoCrAlY inhibited the formation of the coarse flaky particles at the early stage of the milling process. After 5 h of ball milling, the powders remained compact and retained their spherical morphology surrounded by hard Al_2O_3 nanoparticles (Figs. 4(c) and 4(d)). After 15 h of milling, more coarse disks and flakes formed while still being surrounded by hard and dispersed Al_2O_3 nanoparticles (Figs. 4(e) and 4(f)). As the milling time was prolonged up to 25 h, fragmentation of the coarse powders and agglomeration became the dominant mechanisms in this stage to form nanocomposite powders with agglomerated morphology. Finally, with excessive increasing of milling duration (35 h), breakage of the work-hardened nanocomposite particles was the dominant mechanism and fine particles accordingly formed because of their further fracturing induced by ball and wall collisions.

Nevertheless, the creation of relatively large MCrAlY/nano-Al_2O_3 nanocomposite particles might be attributed to their FCC crystal structure in which powder particles may easily deform because of their active slip planes and subsequently weld and join to each other to form coarse agglomerates. Joining of the fine particles was performed by cold welding via the ball/ball or ball/wall collisions in accordance with the investigations accomplished by Ajdelsztajn *et al.* [47] for NiCrAlY coatings and Mercier *et al.* [43] for NiCoCrAlY coatings. However, the particle size and morphology of the milled MCrAlY/nano-Al_2O_3 nanocomposite powders relatively deviated from a spherical shape and may be less than (−45 + 15) μm attained from the commercial MCrAlY powder.

At the beginning stages of mechanical milling, severe plastic deformation may form flaky shape powders [44]. Then, MCrAlY/nano-Al_2O_3 nanocomposite agglomerates with semi-spherical morphology were developed after 25 h of milling. Finally, when the milling duration was prolonged up to 35 h, fracturing may form fine particles with a relatively sharp-edged and angular morphology (Figs. 4(j) and 4(h)) owing to excessive work hardening and subsequent breakage of the milled powders [48].

The structural evolution and morphological transmutation observed in the recent investigation via milling are in accordance with the findings of other researchers for MCrAlY-based coatings [35,38,43,49]. Sharma *et al.* [49] subjected a commercial grade of CoNiCrAlY feedstock powder to mechanical milling and obtained nano-scale CoNiCrAlY powder after 48 h of milling. The average particle size of the developed feedstock was about 5–25 nm. Daroonparvar *et al.* [50] developed nanostructured NiCrAlY powder with a mean particle size of 126.2 nm through atmosphere-controlled mechanical milling.

The presence of ethanol as PCA may prohibit the intensity of cold welding during the progress of mechanical milling. Limited cold welding may occur between processed particles as long as the powder mixture is sufficiently surrounded by PCA during milling at a high-energy rotational speed. Rana *et al.* [51] milled the NiCrAlY powder under a rotational speed of 300 r/min for 14 h. In this research, the toluene solution was used as a PCA to prevent unwanted agglomeration. Afterward, the processed nanostructured powder was deposited using low-velocity oxygen fuel (LVOF) spraying to obtain nanostructured NiCrAlY coating.

The obtained results exemplified that apart from Ni-rich solid solution γ phase, Al_2O_3 nanoparticles with a good dispersion were also detected in the microstructure of the nanocomposite coating. During the mechanical-milling process for the development of nanocomposite powder, the ductile NiCoCrAlY and brittle nano-Al_2O_3 particles were incorporated to form the nanocomposite structure in the powder particles. Hence, in the middle stages of milling, the brittle oxide powders and the work-hardened matrix were broken into fine particles. The mentioned fine particles can cut into the Ni-rich matrix and be surrounded by a ductile γ-phase matrix. As a consequence, a nanocomposite mixture and a nanocrystalline structure were prepared [30,38,52].

In the EDS elemental mapping image (Fig. 5), a relatively uniform distribution of Al_2O_3 nanoparticles in the NiCoCrAlY matrix could be observed in MCrAlY/nano-Al_2O_3 nanocomposite powder. With the contribution of deformation, breakage, cold welding, and agglomeration mechanisms, an optimized nanocomposite powder can be obtained after 25 h of ball milling.

The TEM image in Fig. 7 shows that the microstructure of an MCrAlY/nano-Al_2O_3 nanocomposite powder particle was almost uniform and homogeneous, and numerous black spots were detected in the BF image (Fig. 7(a)). Conversely, bright spot regions in the DF represented the existence of a dispersed nano-scale oxide phase. In this regard, the average grain size was estimated to be 60–80 nm, which is almost in accordance with the crystalline size of the nanocomposite MCrAlY/nano-Al_2O_3 powder measured by the Williamson–Hall method.

4.2. Microstructure of the developed nanocomposite coatings

In practice, the variation between microstructural characteristics of the developed conventional MCrAlY and MCrAlY/nano-Al_2O_3 nanocomposite coatings can be attributed to the difference in temperature and velocity of in-flight particles as reported elsewhere [30]. Indeed, the different behaviors of various types of the prepared nanocomposite powders against HVOF flame heating during the in-flight situation are strongly influenced by the value, distribution, and size of the Al_2O_3 nanoparticles in the Ni-rich γ-phase matrix [42,52−53]. In addition, the morphology and microstructure of the nanocomposite powder can be affected by the structural characteristics and morphology of the starting powders (NiCoCrAlY and developed Al_2O_3 nanoparticles) and by the milling parameters.

Among the three types of the MCrAlY coatings with and without nano-Al_2O_3, the presence of the structural pores and microporosities, as well as considerable unmelted zones in the conventional MCrAlY coating, could be associated with the relatively inadequate localized contact and deformation of droplets onto the surface during HVOF spray deposition (Figs. 8(a) and 8(b)). In another point of view, the nanocomposite coating developed from the processed powder after 35 h of ball milling had higher oxide and porosity contents than the other counterparts (Figs. 8(e) and 8(f) and Fig. 9(c)). Indeed, the disk-shaped particles had a great tendency to absorb and react with oxygen during time-of-flight, especially the more active elements (e.g., Al and Y). Moreover, the specific heat of in-flight particles may increase because of their nano-scale structure that may intensify the oxidation of the melted powders during time-of-flight (He & Lavernia, 2001).

Compared with the other types of coatings, the MCrAlY/nano-Al_2O_3 nanocomposite coating developed from milled powder obtained an optimum coating microstructure after 25 h because of its semi-spherical and agglomerated morphology. As a result, the agglomerated particles were completely flattened and adhered to the surface from a relatively dense structure with a low amount of defects and inhomogeneities.

5. Conclusions

(1) Al_2O_3 nanoparticles were successfully prepared from the commercial micron-sized powder via high-energy ball milling under 300 r/min after 48 h.

(2) Williamson–Hall plot analysis showed that the crystallite size of the ball-milled Al_2O_3 nanocomposite powder after 48 h is smaller than that of the other conventional and nanocomposite powder.

(3) The calculated lattice strain of the ball-milled Al_2O_3 powder increased slightly because of the plastic deformation and breakage of the powders during ball milling.

(4) Al_2O_3 nanoparticles dispersed well into MCrAlY after 15 and 25 h of high-energy ball milling. As the milling time was prolonged, the morphology of the nanocomposite powders changed to flaky and crashed, and the mean particle size decreased accordingly.

(5) Structural homogeneity and density of the MCrAlY/nano-Al_2O_3 coating prepared after 25 h of ball-milling was much higher than that of the counterpart without nano-Al_2O_3 reinforcement.

Acknowledgements

This work was supported by the Department of Materials Engineering, Tarbiat Modares University, Iran. The first author is also grateful to Mr. Mohammad Amin Davoudabadi for the final proofreading the article.

References

[1] C.U. Hardwicke and Y.C. Lau, Advances in thermal spray coatings for gas turbines and energy generation: A review, *J. Therm. Spray Technol.*, 22(2013), No. 5, p. 564.

[2] G. Pulci, J. Tirillò, F. Marra, F. Sarasini, A. Bellucci, T. Valente, and C. Bartuli, High temperature oxidation and microstructural evolution of modified MCrAlY coatings, *Metall. Mater. Trans. A*, 45(2014), No. 3, p. 1401.

[3] D.R.G. Achar, R. Munoz-Arroyo, L. Singheiser, and W.J. Quadakkers, Modelling of phase equilibria in MCrAlY coating systems, *Surf. Coat. Technol.*, 187(2004), No. 2, p. 272.

[4] I. Taie, A. Al-Shahrani, N. Qari, A. Fihri, W. Al-Obaid, and G. Alabedi, High temperature corrosion resistant coatings for gas flare systems, *Ceram. Int.*, 44(2018), No. 5, p. 5124.

[5] H.R. Abedi, M. Salehi, and A. Shafyei, Mechanical and thermal properties of double-layer and triple-layer thermal barrier coatings with different ceramic top coats onto polyimide matrix composite, *Ceram. Int.*, 43(2017), No. 15, p. 12770.

[6] A. Jam, S.M.R. Derakhshandeh, H. Rajaei, and A.H. Pakseresht, Evaluation of microstructure and electrochemical behavior of dual-layer NiCrAlY/mullite plasma sprayed coating on high silicon cast iron alloy, *Ceram. Int.*, 43(2017), No. 16, p. 14146.

[7] F. Ghadami and A.Sabour Rouh Aghdam, Improvement of high velocity oxy-fuel spray coatings by thermal post-treatments: A critical review, *Thin Solid Films*, 678(2019), p. 42.

[8] D. Kumar, K.N. Pandey, and D.K. Das, Microstructure studies of air-plasma-spray-deposited conicraly coatings before and after thermal cyclic loading for high-temperature application, *Int. J. Miner. Metall. Mater.*, 23(2016), No. 8, p. 934.

[9] G.L. Hou, Y.L. An, X.Q. Zhao, H.D. Zhou, and J.M. Chen, Effect of alumina dispersion on oxidation behavior as well as friction and wear behavior of hvof-sprayed CoCrAlYTaCSi coating at elevated temperature up to 1000°C, *Acta Mater.*, 95(2015), p. 164.

[10] L. D. Zhao and E. Lugscheider, High velocity oxy-fuel spraying of a NiCoCrAlY and an intermetallic NiAl−TaCr alloy, *Surf. Coat. Technol.*, 149(2002), No. 2, p. 230.

[11] L. Fan, H.Y. Chen, Y.H. Dong, L.H. Dong, and Y.S. Yin, Wear and corrosion resistance of laser-cladded Fe-based composite coatings on AISI 4130 steel, *Int. J. Miner. Metall. Mater.*, 25(2018), No. 6, p. 716.

[12] C. Tao, L. Wang, and X. Song, High-temperature frictional wear behavior of MCrAlY-based coatings deposited by atmosphere plasma spraying, *Int. J. Miner. Metall. Mater.*, 24(2017), No. 2, p. 222.

[13] K. Jithesh and M. Arivarasu, Comparative studies on the hot corrosion behavior of air plasma spray and high velocity oxygen fuel coated Co-based L605 superalloys in a gas turbine environment, *Int. J. Miner. Metall. Mater.*, 27(2020), No. 5, p. 649.

[14] M.J. Tobar, J.M. Amado, A. Yáñez, J.C. Pereira, and V. Amigó, Laser cladding of MCrAlY coatings on stainless steel, *Phys. Procedia*, 56(2014), p. 276.

[15] T. Huang, J. Bergholz, G. Mauer, R. Vassen, D. Naumenko, and W.J. Quadakkers, Effect of test atmosphere composition on high-temperature oxidation behaviour of CoNiCrAlY coatings produced from conventional and ODS powders, *Mater. High Temp.*, 35(2018), No. 1-3, p. 97.

[16] J. Bergholz, B.A. Pint, K.A. Unocic, and R. Vaßen, Fabrication of oxide dispersion strengthened bond coats with low Al_2O_3 content, *J. Therm. Spray Technol.*, 26(2017), No. 5, p. 868.

[17] F. Ghadami, M.H. Sohi, and S. Ghadami, Effect of bond coat and post-heat treatment on the adhesion of air plasma sprayed WC-Co coatings, *Surf. Coat. Technol.*, 261(2015), p. 289.

[18] F. Ghadami, S. Ghadami, and H. Abdollah-Pour, Structural and oxidation behavior of atmospheric heat treated plasma sprayed WC-Co coatings, *Vacuum*, 94(2013), p. 64.

[19] F. Ghadami, A. Sabour Rouh Aghdam, S. Ghadami, and Q. Zeng, Effect of vacuum heat treatment on the oxidation kinetics of freestanding nanostructured NiCoCrAlY coatings deposited by high-velocity oxy-fuel spraying, *J. Vac. Sci. Technol. A*, 38(2020), No. 2, art. No. 022601.

[20] F. Ghadami, A. Sabour Rouh Aghdam, and S. Ghadami, Abrasive wear behavior of nano-ceria modified NiCoCrAlY coatings deposited by the high-velocity oxy-fuel process, *Mater. Res. Express*, 6(2020), No. 12, p. 1250d6.

[21] M. Heydarzadeh Sohi and F. Ghadami, Comparative tribological study of air plasma sprayed WC−12%Co coating versus conventional hard chromium electrodeposit, *Tribol. Int.*, 43(2010), No. 5, p. 882.

[22] S. Ghadami, E. Taheri-Nassaj, H.R. Baharvandi, and F. Ghadami, Effect of SiC and $MoSi_2$ in situ phases on the oxidation behavior of HfB_2-based composites, *Ceram. Int.*, 46(2020), No. 12, p. 20299.

[23] A. Sayyadi-Shahraki, S.M. Rafiaei, S. Ghadami, and K.A. Nekouee, Densification and mechanical properties of spark plasma sintered Si_3N_4/ZrO_2 nano-composites, *J. Alloys Compd.*, 776(2019), p. 798.

[24] S. Ghadami, E. Taheri-Nassaj, and H.R. Baharvandi, Novel HfB_2−SiC−$MoSi_2$ composites by reactive spark plasma sintering, *J. Alloys Compd.*, 809(2019), p. 151705.

[25] S. Ghadami, H.R. Baharvandi, and F. Ghadami, Influence of the vol% SiC on properties of pressureless Al_2O_3/SiC nanocomposites, *J. Compos. Mater.*, 50(2016), No. 10, p. 1367.

[26] S. Ghadami, E. Taheri-Nassaj, H.R. Baharvandi, and F. Ghadami, Effect of in situ VSi_2 and SiC phases on the sintering behavior and the mechanical properties of HfB_2-based composites, *Sci. Rep.*, 10(2020), No. 1, p. 16540.

[27] F. Ghadami, M. Heydarzadeh Sohi, and S. Ghadami, Effect of TIG surface melting on structure and wear properties of air plasma-sprayed WC−Co coatings, *Surf. Coat. Technol.*, 261(2015), p. 108.

[28] K. Bobzin, T. Schläfer, K. Richardt, and M. Brühl, Develop-

ment of oxide dispersion strengthened MCrAlY coatings, *J. Therm. Spray Technol.*, 17(2008), p. 853.
[29] F. Tang, L. Ajdelsztajn, and J.M. Schoenung, Influence of cryomilling on the morphology and composition of the oxide scales formed on hvof CoNiCrAlY coatings, *Oxid. Met.*, 61(2004), No. 3, p. 219.
[30] F. Ghadami, A. Zakeri, A.S.R. Aghdam, and R. Tahmasebi, Structural characteristics and high-temperature oxidation behavior of HVOF sprayed nano-CeO_2 reinforced NiCoCrAlY nanocomposite coatings, *Surf. Coat. Technol.*, 373(2019), p. 7.
[31] F. Ghadami and A.S. Rouh Aghdam, Preparation of NiCrAlY/nano-CeO_2 powder with the core-shell structure using high-velocity oxy-fuel spraying process, *Mater. Chem. Phys.*, 243(2020), art. No. 122551.
[32] S. Ghadami S, E. Taheri-Nassaj, H.R. Baharvandi and F. Ghadami, Improvement of mechanical properties of HfB 2-based composites by incorporating in situ SiC reinforcement through pressureless sintering, *Sci. Rep.*, 11(2021), art. No. 9835.
[33] M. Sameezadeh, H. Farhangi, and M. Emamy, Structural characterization of AA 2024-$MoSi_2$ nanocomposite powders produced by mechanical milling, *Int. J. Miner. Metall. Mater.*, 20(2013), No. 3, p. 298.
[34] B. Li, J. Jia, Y. Gao, M. Han, and W. Wang, Microstructural and tribological characterization of NiAl matrix self-lubricating composite coatings by atmospheric plasma spraying, *Tribol. Int.*, 109(2017), p. 563.
[35] Z. Khodsiani, H. Mansuri, and T. Mirian, The effect of cryomilling on the morphology and particle size distribution of the NiCoCrAlYSi powders with and without nano-sized alumina, *Powder Technol.*, 245(2013), p. 7.
[36] R.A. Mahesh, R. Jayaganthan, and S. Prakash, A study on the oxidation behavior of HVOF sprayed NiCrAlY–0.4wt.% CeO_2 coatings on superalloys at elevated temperature, *Mater. Chem. Phys.*, 119(2010), No. 3, p. 449.
[37] S. Kamal, R. Jayaganthan, and S. Prakash, Mechanical and microstructural characteristics of detonation gun sprayed NiCrAlY+0.4wt% CeO_2 coatings on superalloys, *Mater. Chem. Phys.*, 122(2010), No. 1, p. 262.
[38] F. Ghadami, A. Sabour Rouh Aghdam, A. Zakeri, B. Saeedi, and P. Tahvili, Synergistic effect of CeO_2 and Al_2O_3 nanoparticle dispersion on the oxidation behavior of MCrAlY coatings deposited by HVOF, *Ceram. Int.*, 46(2020), No. 4, p. 4556.
[39] F. Ghadam, A.S. Rouh Aghdam, and S. Ghadami, Preparation, characterization and oxidation behavior of CeO_2-gradient NiCrAlY coatings applied HVOF thermal spraying process, *Ceram. Int.*, 46(2020), No. 12, p. 20500.
[40] G.K. Williamson and W.H. Hall, X-ray line broadening from filed aluminium and wolfram, *Acta Metall.*, 1(1953), No. 1, p. 22.
[41] E.M. Anghel, M. Marcu, A. Banu, I. Atkinson, A. Paraschiv, and S. Petrescu, Microstructure and oxidation resistance of a NiCrAlY/Al_2O_3-sprayed coating on Ti−19Al−10Nb−V alloy, *Ceram. Int.*, 42(2016), No. 10, p. 12148.
[42] M. Tahari, M. Shamanian, and M. Salehi, Microstructural and morphological evaluation of MCrAlY/YSZ composite produced by mechanical alloying method, *J. Alloys Compd.*, 525(2012), p. 44.
[43] D. Mercier, B.D. Gauntt, and M. Brochu, Thermal stability and oxidation behavior of nanostructured NiCoCrAlY coatings, *Surf. Coat. Technol.*, 205(2011), No. 17-18, p. 4162.
[44] C. Suryanarayana, Mechanical alloying and milling, *Prog. Mater Sci.*, 46(2001), No. 1-2, p. 1.
[45] S. Saeidi, K.T. Voisey, and D.G. McCartney, The effect of heat treatment on the oxidation behavior of HVOF and VPS CoNiCrAlY coatings, *J. Therm. Spray Technol.*, 18(2009), No. 2, p. 209.
[46] R. Sachan and J.W. Park, Formation of nanodispersoids in Fe–Cr–Al/30%TiB_2 composite system during mechanical alloying, *J. Alloys Compd.*, 485(2009), No. 1-2, p. 724.
[47] L. Ajdelsztajn, J.A. Picas, G.E. Kim, F.L. Bastian, J. Schoenung, and V. Provenzano, Oxidation behavior of HVOF sprayed nanocrystalline NiCrAlY powder, *Mater. Sci. Eng. A*, 338(2002), No. 1-2, p. 33.
[48] C. Suryanarayana, Synthesis of nanocomposites by mechanical alloying, *J. Alloys Compd.*, 509(2011), p. S229.
[49] P. Sharma and J. Dutta Majumdar, Studies on nano-crystalline CoNiCrAlY consolidated by conventional and microwave sintering, *Adv. Powder Technol.*, 27(2016), No. 1, p. 72.
[50] M. Daroonparvar, M.S. Hussain, and M.A.M. Yajid, The role of formation of continues thermally grown oxide layer on the nanostructured NiCrAlY bond coat during thermal exposure in air, *Appl. Surf. Sci.*, 261(2012), p. 287.
[51] N. Rana, M.M. Mahapatra, R. Jayaganthan, and S. Prakash, Deposition of nanocrystalline coatings by modified LVOF thermal spray method, *J. Alloys Compd.*, 615(2014), p. 779.
[52] L.D. Zhao, M. Parco, and E. Lugscheider, Wear behaviour of Al_2O_3 dispersion strengthened MCrAlY coating, *Surf. Coat. Technol.*, 184(2004), No. 2-3, p. 298.
[53] F. Ghadami, A. Sabour Rouh Aghdam, and S. Ghadami, Mechanism of the oxide scale formation in thermally-sprayed NiCoCrAlY coatings modified by CeO_2 nanoparticles, *Mater. Today Commun.*, 24(2020), p. 101357.